



HAL
open science

Diamond formation kinetics in shock-compressed C H O samples recorded by small-angle x-ray scattering and x-ray diffraction

Zhiyu He, Melanie Rödel, Julian Lütgert, Armin Bergermann, Mandy Bethkenhagen, Deniza Chekrygina, Thomas Cowan, Adrien Descamps, Martin French, Eric Galtier, et al.

► To cite this version:

Zhiyu He, Melanie Rödel, Julian Lütgert, Armin Bergermann, Mandy Bethkenhagen, et al.. Diamond formation kinetics in shock-compressed C H O samples recorded by small-angle x-ray scattering and x-ray diffraction. *Science Advances* , 2022, 8 (35), pp.eabo0617. 10.1126/sciadv.abo0617. hal-04946776

HAL Id: hal-04946776

<https://hal.science/hal-04946776v1>

Submitted on 13 Feb 2025

HAL is a multi-disciplinary open access archive for the deposit and dissemination of scientific research documents, whether they are published or not. The documents may come from teaching and research institutions in France or abroad, or from public or private research centers.

L'archive ouverte pluridisciplinaire **HAL**, est destinée au dépôt et à la diffusion de documents scientifiques de niveau recherche, publiés ou non, émanant des établissements d'enseignement et de recherche français ou étrangers, des laboratoires publics ou privés.



Distributed under a Creative Commons Attribution 4.0 International License

APPLIED PHYSICS

Diamond formation kinetics in shock-compressed C—H—O samples recorded by small-angle x-ray scattering and x-ray diffraction

Zhiyu He^{1,2,3*}, Melanie Rödel^{1,4}, Julian Lütgert^{1,2,4}, Armin Bergermann², Mandy Bethkenhagen⁵, Deniza Chekrygina¹, Thomas E. Cowan^{1,4}, Adrien Descamps⁶, Martin French², Eric Galtier⁶, Arianna E. Gleason⁶, Griffin D. Glenn^{6,7}, Siegfried H. Glenzer⁶, Yuichi Inubushi^{8,9}, Nicholas J. Hartley⁶, Jean-Alexis Hernandez^{10,11}, Benjamin Heuser^{1,2}, Oliver S. Humphries¹, Nobuki Kamimura¹², Kento Katagiri¹², Dimitri Khaghani⁶, Hae Ja Lee⁶, Emma E. McBride⁶, Kohei Miyanishi⁹, Bob Nagler⁶, Benjamin Ofori-Okai⁶, Norimasa Ozaki^{12,13}, Silvia Pandolfi⁶, Chongbing Qu², Divyanshu Ranjan^{1,2}, Ronald Redmer², Christopher Schoenwaelder^{6,14}, Anja K. Schuster^{1,4}, Michael G. Stevenson², Keiichi Sueda⁹, Tadashi Togashi^{8,9}, Tommaso Vinci¹⁵, Katja Voigt^{1,4}, Jan Vorberger¹, Makina Yabashi^{8,9}, Toshinori Yabuuchi^{8,9}, Lisa M. V. Zinta², Alessandra Ravano¹⁵, Dominik Kraus^{1,2*}

Extreme conditions inside ice giants such as Uranus and Neptune can result in peculiar chemistry and structural transitions, e.g., the precipitation of diamonds or superionic water, as so far experimentally observed only for pure C—H and H₂O systems, respectively. Here, we investigate a stoichiometric mixture of C and H₂O by shock-compressing polyethylene terephthalate (PET) plastics and performing *in situ* x-ray probing. We observe diamond formation at pressures between 72 ± 7 and 125 ± 13 GPa at temperatures ranging from ~ 3500 to ~ 6000 K. Combining x-ray diffraction and small-angle x-ray scattering, we access the kinetics of this exotic reaction. The observed demixing of C and H₂O suggests that diamond precipitation inside the ice giants is enhanced by oxygen, which can lead to isolated water and thus the formation of superionic structures relevant to the planets' magnetic fields. Moreover, our measurements indicate a way of producing nanodiamonds by simple laser-driven shock compression of cheap PET plastics.

INTRODUCTION

Ice giant planets such as Neptune and Uranus are highly abundant in our galaxy (1). The interiors of these celestial objects are thought to be mainly composed of a dense fluid mixture of water, methane, and ammonia (2). Because of the high pressures and temperatures deep inside these planets, the material mixture will likely undergo chemical reactions and structural transitions (3–5). An example of these reactions is the possible dissociation of hydrocarbons (6) and subsequent phase separation, allowing the formation of diamonds (7) and presumably metallic hydrogen or superionic water (3, 8), which may act as a heat source and help to explain the generation of the unique magnetic fields modeled for the ice giants (9–11).

¹Helmholtz-Zentrum Dresden-Rossendorf, Bautzner Landstrasse 400, 01328 Dresden, Germany. ²Institut für Physik, Universität Rostock, Albert-Einstein-Str. 23-24, 18059 Rostock, Germany. ³Shanghai Institute of Laser Plasma, 201800 Shanghai, China. ⁴Technische Universität Dresden, 01069 Dresden, Germany. ⁵École Normale Supérieure de Lyon, Laboratoire de Géologie de Lyon, LGLTPE UMR 5276, Centre Blaise Pascal, 46 allée d'Italie, Lyon 69364, France. ⁶SLAC National Accelerator Laboratory, Menlo Park, CA 94025, USA. ⁷Stanford University, Stanford, CA 94305, USA. ⁸Japan Synchrotron Radiation Research Institute, 1-1-1 Kouto, Sayo-cho, Sayo-gun, Hyogo 679-5198, Japan. ⁹RIKEN SPring-8 Center, 1-1-1 Kouto, Sayo-cho, Sayo-gun, Hyogo 679-5148, Japan. ¹⁰Centre for Earth Evolution and Dynamics, University of Oslo, N-0315 Oslo, Norway. ¹¹European Synchrotron Radiation Facility, 71 avenue des Martyrs, 38000 Grenoble, France. ¹²Graduate School of Engineering, Osaka University, Suita, Osaka 565-0871, Japan. ¹³Institute of Laser Engineering, Osaka University, Suita, Osaka 565-0871, Japan. ¹⁴Erlangen Centre for Astroparticle Physics, Friedrich-Alexander-Universität Erlangen Nürnberg, Erwin-Rommel-Str 1, 91058 Erlangen, Germany. ¹⁵LULI, CNRS, CEA, Sorbonne Université, Ecole Polytechnique–Institut Polytechnique de Paris, F-91128 Palaiseau, France.

*Corresponding author. Email: zhiyu.he@uni-rostock.de (Z.H.); dominik.kraus@uni-rostock.de (D.Kr.)

Recent laser shock experiments on polystyrene [PS; (C₈H₈)_n] in combination with x-ray techniques have provided the first *in situ* evidence for the formation of diamonds in compressed hydrocarbons at planetary-relevant states in the laboratory (12–14). However, the presence of water and therefore large amounts of oxygen needs to be considered for further conclusions on processes inside the ice giants. Thus, investigating C—H—O samples provides a more realistic scenario than studying pure hydrocarbon or water systems (15). A separation of carbon from H₂O is likely required for a superionic phase of water to be present inside Neptune and/or Uranus (3). If carbon would form bonds with oxygen, such structures, which could help to explain the peculiar magnetic field observed for both planets, may be inhibited.

Thanks to the advent of x-ray free-electron laser (XFEL) facilities and increasingly mature experimental capabilities, probing the internal structure of materials under dynamic compression to mimic planetary interiors has seen tremendous progress in recent years. While x-ray diffraction (XRD) identifies crystalline and liquid correlations on the angstrom level, small-angle x-ray scattering (SAXS) (16) is sensitive to feature sizes on the order of 1 to 100 nm. Therefore, combining SAXS and XRD in a single experiment has a great potential to enable accurate measurements of the nanodiamond size distribution and nucleation process initiated inside the plastic samples, which provides direct access to the kinetics of the carbon-hydrogen phase separation reaction relevant to the interiors of planets (13).

Here, the size distribution and the growth process of nanodiamonds, created from shock-compressed polyethylene terephthalate [PET; (C₁₀H₈O₄)_n], stoichiometrically a mixture of carbon and

Copyright © 2022 The Authors, some rights reserved; exclusive licensee American Association for the Advancement of Science. No claim to original U.S. Government Works. Distributed under a Creative Commons Attribution License 4.0 (CC BY).

Downloaded from https://www.science.org on March 06, 2023

H₂O], are characterized by in situ XRD and SAXS consistently at two different XFEL facilities, which shows the importance of the pressure P –temperature T state on the diamond formation kinetics. Standard velocity interferometer for any reflector (VISAR) diagnostics and the recently published equation of state data for PET (15) are applied to estimate the P - T state of the shocked PET sample, allowing us to compare the XRD data to density functional theory molecular dynamics (DFT-MD) simulations, where they show excellent agreement. Our results provide insights of unprecedented quality into chemistry relevant to planetary interiors and the general capabilities for simultaneously characterizing structural transitions on both angstrom and nanometer scale in dynamic compression experiments. At the same time, as diamond formation is achieved by a single-shock compression in contrast to more elaborate compression histories required in previous experiments (12), our study points toward a new way to efficiently produce nanodiamonds using cheap PET plastics as initial material.

RESULTS

Experimental method

We performed the discussed experiments at two different XFEL facilities: the Matter in Extreme Conditions (MEC) endstation of the Linac Coherent Light Source (LCLS) of SLAC National Accelerator Laboratory (17, 18) (Fig. 1) and the Spring-8 Angstrom Compact free electron Laser (SACLA) (19, 20). At LCLS, the structural changes and density variations of compressed PET can be observed by in situ XRD and SAXS with the LCLS pulse of 9.5-keV photon energy and 50-fs duration. The XRD and SAXS detectors were capable of recording single-photon events, and the data were integrated

azimuthally after masking the beamstop and the parasitic scattering. More details on the experimental setup and the applied diagnostics can be found in Materials and Methods. A similar setup was used at SACLA and is depicted in fig. S1 of the Supplementary Materials.

Examples of raw data images from XRD and SAXS from PET under ambient conditions and a shocked state are illustrated in Fig. 1. Shocked and ambient data apply the same color scale per diagnostic. The drive laser ablates the aluminum coating that is visible in the XRD lineouts of cold PET samples. Hence, these peaks disappear for driven targets (see Fig. 1). In the shocked state, the symmetric scattering characteristic of ambient PET in the SAXS image vanishes. In turn, the SAXS signal increases strongly in the higher-wave number q range of the detector and results in a bright ring-shaped feature, which corresponds to the pattern consistent with densely packed nanospheres (21). Contemporaneously, strong diamond diffraction is observed by XRD, which demonstrates the formation of nanodiamonds being traceable by two complementary x-ray techniques.

Diamond formation kinetics

Figure 2 depicts the temporal evolution of 100- μ m PET samples shock-compressed to \sim 100 GPa at the LCLS in the form of raw in situ XRD and in situ SAXS data with their corresponding azimuthally integrated lineouts. The individual pressures were determined by measuring the shock velocity and using the known PET Hugoniot curve (15). In each XRD lineout, the diamond (111) peak illustrated by the shaded area was modeled to be approximately Lorentzian, while the signal below is given by the contribution of a liquid C–H–O mixture, which is well represented by a Gaussian in the k range below the diamond peak (14). The Gaussian shape is also in

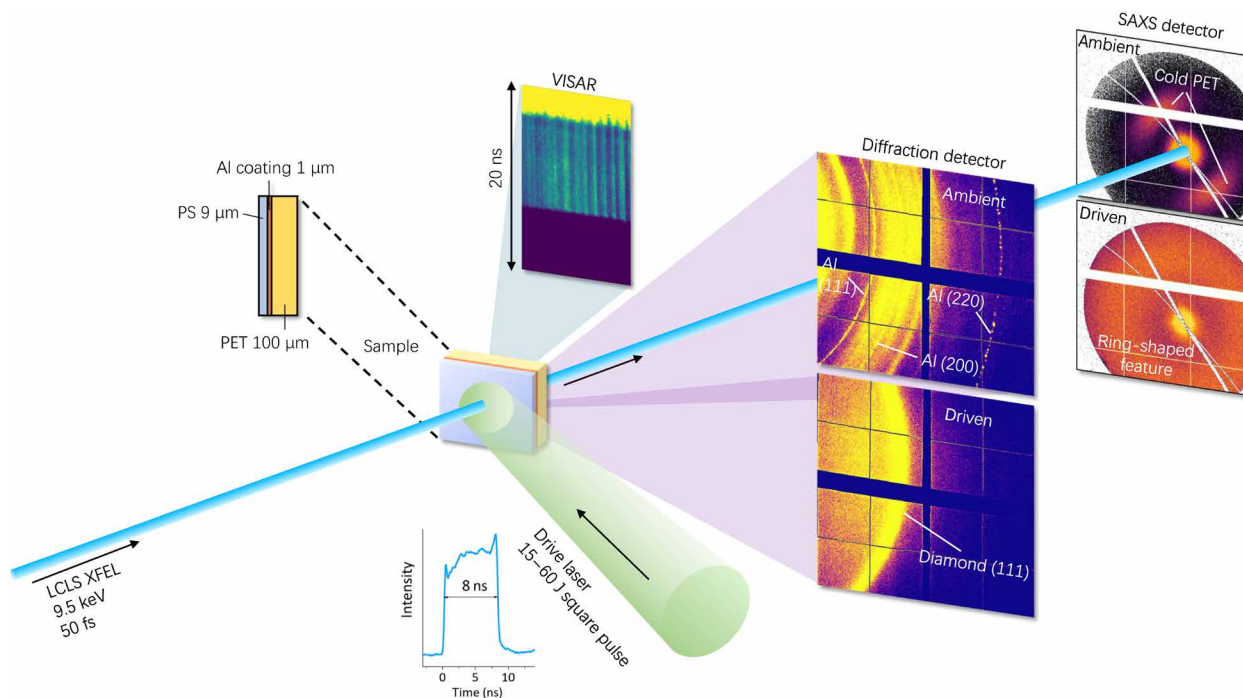


Fig. 1. Schematic of the experimental setup combining XRD, SAXS, and VISAR at the MEC endstation of LCLS. Raw XRD and SAXS data under ambient and driven conditions of PET are presented. The SAXS is centered around the direct XFEL beam, with high-Z wires used to block the zero momentum-transfer peak. Images under ambient and driven conditions apply the same color scale.

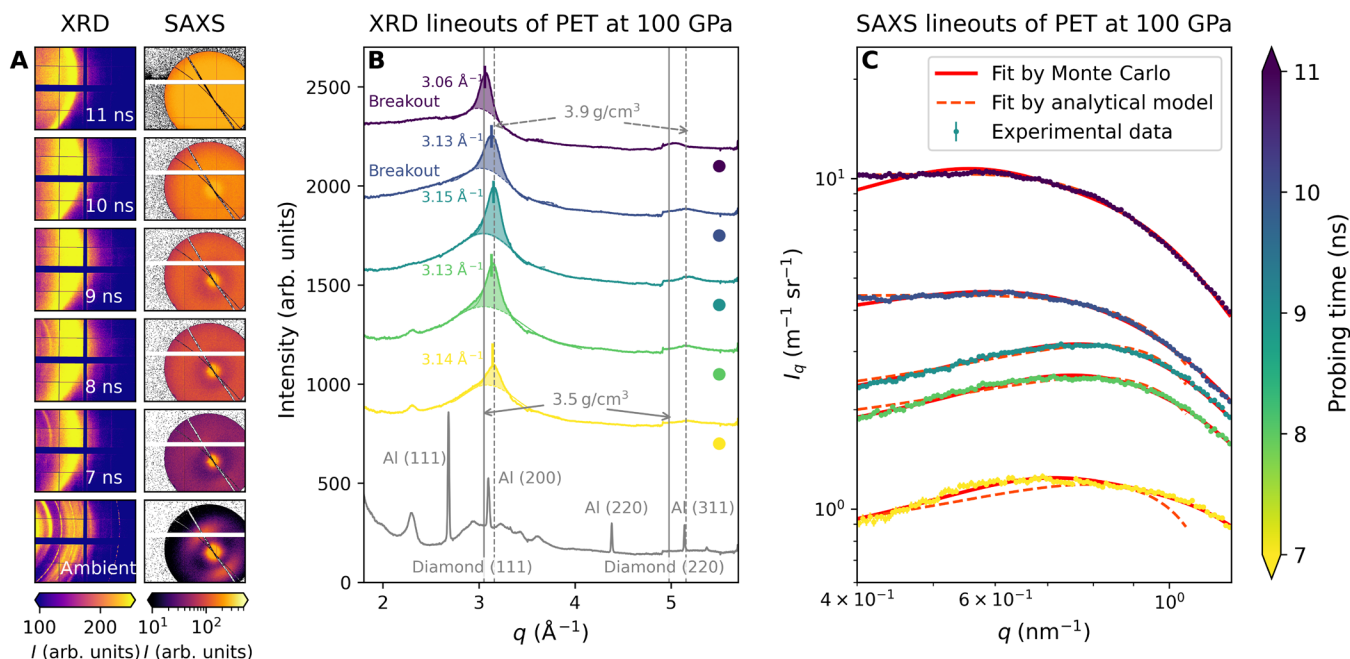


Fig. 2. XRD and SAXS results of a 100- μm PET measured at the LCLS with different time delays. (A) Raw XRD and SAXS images and corresponding azimuthally integrated lineouts of (B) XRD and (C) SAXS with increasing pump-probe delay time at around 100 GPa (with laser energies of ~ 36 J). Offsets of the intensities are applied to different probing time in XRD indicated by the filled colored dots. The dominant error in SAXS lineouts is the Poisson error (58). The fit curves from two SAXS analysis methods (see Materials and Methods for details) are plotted.

good agreement with DFT-MD simulations of the liquid (see Materials and Methods and Supplementary Materials for more details). Due to the experimental geometry, the signal-to-background ratio of the diamond (220) peak is substantially lower than for the (111) reflection. As the (220) peak also sits on top of a liquid correlation peak, the solid contribution is difficult to distinguish quantitatively from the background. Thus, the analysis of the formation characteristics of the nanodiamonds mainly focuses on the more prominent (111) peak. We use the Lorentzian fit to obtain the center and the width of the diamond (111) peak. The Scherrer formula (22) was then applied to estimate the minimum crystallite size of a few nanometers based on the width of the diamond Bragg peak of around 0.2 \AA^{-1} . This value is considerably smaller than the peak width of the liquid mixture peak of $1\text{--}2 \text{ \AA}^{-1}$ by Lütgert *et al.* (15) and estimations from DFT-MD simulations. With this clear feature separation, the diamond fraction (the absolute amount of carbon atoms in the shock-compressed PET foil that ended up in diamond lattices) was estimated from the diamond peak integral between the liquid peak and the experimental data (14). The diamond diffraction peak area increases with proceeding time during the compression process before shock breakout at the sample rear side (it refers to the cases when the probing times are at 7, 8, and 9 ns since the breakout time at ~ 100 GPa is about 9.8 ns). Compressed diamond densities of up to 3.87 g/cm^3 were deduced from the position of the diamond Bragg peak at $3.14 \pm 0.01 \text{ \AA}^{-1}$ compared to the ambient diamond density of 3.51 g/cm^3 at 3.05 \AA^{-1} . The diamond peak area steps increasing after shock breakout, and the peak position moves back to lower q ($\sim 3.06 \text{ \AA}^{-1}$) as the crystallites are relaxing to ambient density. In SAXS, a substantial increase in total scattering intensity for the progressing shock wave is observed when diamond formation can be seen in XRD data. The described SAXS ring feature is

not visible for drives where no diamond formation has been observed. Therefore, the signal is assumed to be generated by the nanodiamonds where both the relative volume fraction and the size distribution of the crystallites affect the overall shape and intensity of the SAXS signal. SAXS is also sensitive to demixing processes without the formation of crystalline structures, as long as density differences are present between the separated states. Therefore, we can conclude that at pressures below and above the conditions where diamond formation is observed, our sample remains in a mixed state.

The high-quality SAXS signals obtained by the detector allow the nanoparticle size distribution to be deduced. Here, we use two different methods for SAXS data analysis (see Materials and Methods and Supplementary Materials for details on the applied methods). Figure 3 shows the obtained nanoparticle distribution derived from the SAXS lineouts in Fig. 2C. As an analytical model, we assumed a Schulz distribution (23, 24) with the polydispersity $p = \sigma/R \approx 0.1$, where the effective radius R was obtained by fitting the shape of the SAXS lineouts, and σ was the root mean square deviation from R . Because of the high data quality and a sufficient q range, the radius distribution of the nanodiamonds can also be obtained by Monte Carlo methods without assuming a specific distribution function. Here, the mean radius of particles increases from 1.6 to 2 nm with increasing delay time between the drive laser and x-ray probe. After the shock breakout, which results in a pressure release of the partially solid and liquid system, the Monte Carlo results indicate that the radius distribution becomes highly dispersed (see Fig. 3). At this stage, the analytical model results in systematically larger effective radii. However, the simple assumption of a Schulz distribution for moderately dispersed systems seems no longer valid at this point. In summary, the growth of the mean particle size with progressing

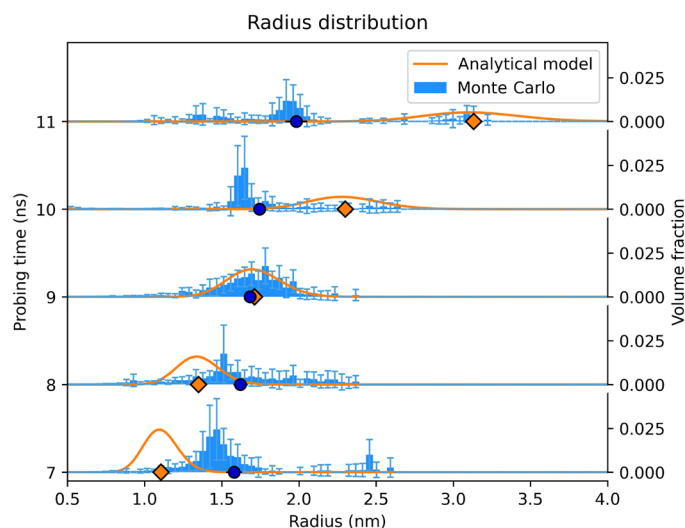


Fig. 3. Radius distribution of nanoparticles with compression history. The radius distribution was extracted from the Monte Carlo method and the analytical model corresponding to the SAXS lineouts in Fig. 2C. Dark blue dots and orange diamonds represent the mean radius of the Monte Carlo method and the effective radius of the analytical model, respectively. The uncertainty in the mean radius of the Monte Carlo method comes from the SDs for the individual bars, describing the convergence of the Monte Carlo method.

shock propagation has been observed by both methods, indicating that the nanodiamonds increase their size until the shock breakout releases the high-pressure conditions.

Effect of pressure

PET samples were driven to different shock pressures by varying the pulse energy of the drive laser to investigate the effect of pressure and temperature on the diamond formation in shock-compressed C–H–O samples. At pressures below 74 GPa, both XRD and SAXS data did not show diamond formation. For intermediate pressures between 74 and 125 GPa, diamond features are present in the data. However, they disappear above 125 GPa. At this upper bound in pressure, temperatures approach the diamond melting line (25), reaching approximately 6000 K along the PET Hugoniot (15). Results from the different facilities, LCLS and SACLA, provide excellent agreement on this observation, which reduces a potential effect of systematic errors in the individual experimental setups.

Using DFT-MD simulations, we can compare our experimental XRD lineouts with calculated diffraction patterns of the compressed C–H–O mixtures with various carbon-to-water ratios at different pressures along the PET Hugoniot. The simulated patterns are reasonably consistent with the residual liquid structure and inferred temperatures from our experimental data (see Materials and Methods and Supplementary Materials for more details).

It is observed that the SAXS intensity during shock propagation is directly correlated to the diamond content recorded by XRD (see fig. S3 for details). Moreover, data from both SAXS analysis methods consistently showed evidence that the nanodiamond particle sizes grow with increasing pressure (see fig. S4 for details). One reasonable explanation is that high pressure promotes and accelerates the growth of the particle size, resulting in a larger size at higher pressure as probed by x-ray techniques during the propagation of shock waves with various intensities through samples of the same thickness.

DISCUSSION

Using XRD, we were able to confirm the diamond formation from compressed PET in laser-driven shock experiments. In SAXS data, a prominent signal was observed that we identified with nanoparticles with several nanometers in diameter. Since this feature occurred when a strong diamond signal was detected in in situ XRD data, we infer that the nanoparticles observed in SAXS are likely to be diamond crystals. Therefore, SAXS provides a sensitive instrument to study diamond formation in shock-compressed experiments, even when the signal of nanoparticles is weak and XRD is impeded by the liquid background peak. These findings were reproduced over different target materials and different setups at different international laser facilities (LCLS and SACLA).

In Fig. 4, our results for shock-compressed PET are illustrated in a phase diagram together with previous data from PS (12), models for planetary interiors (4, 26–28), theoretical predictions for diamond melting (25), and C–H phase separation (29) as well as the assumed hydrogen insulator-metal transition (30). The data points where we observe diamond formation in plastics are marked by diamond symbols in the purple shaded area. This area overlaps with the predicted isentropes of Uranus and Neptune (26) (represented by only one curve because of the small differences), but is a little bit higher in temperature than the more recent models (4, 27), and slightly intersects the recently predicted isentrope for Jupiter (28). In PET, diamond forms under P - T conditions where no C–H separation has been observed for PS on the principal Hugoniot. As the temperature on the PET Hugoniot is only marginally smaller, especially at lower pressures, this suggests that the oxygen atoms in PET are key for explaining the difference, in agreement with first-principles studies of mixtures relevant to the interiors of ice giants (3). In the first-principles studies, it was found that the presence of O increases the lifetimes of C–C bonds, resulting in the clustering of C atoms and the demixing of the liquid mixtures in such environments (3).

Moreover, our results of P - T conditions for diamond formation roughly coincide with the insulator-metal transition of liquid hydrogen suggested by theoretical (30) and experimental studies (31–35), which may indicate a direct correlation. The differences between the PS and PET results, however, point toward a substantial influence of the initial composition on chemistry under extreme conditions. In this case, our study demonstrates that the presence of oxygen supports diamond formation, which is therefore likely to occur inside planets of the corresponding composition. If carbon would be oxidized, diamond formation would have been reduced in our experiment in comparison to the pure C–H data. As the opposite is observed, it can be concluded that oxygen supports rather than inhibits C–H separation. The subsequent carbon precipitation can then act as a heat source inside ice giants, leading to a carbon-rich layer around the core. Carbon separating from H and O also increases the likelihood for regions of superionic water and/or metallic hydrogen being present inside the ice giants (3, 36), which may help to explain the peculiar magnetic fields observed for those planets.

Our study has shown that simultaneous use of in situ x-ray methods in dynamic compression experiments at XFEL facilities provides insight of unprecedented quality into the peculiar chemistry deep inside planets to obtain a better understanding of our Solar System and the vast number of exoplanets found in the orbit of other stars. In particular, the demonstrated experimental platform can be used to investigate various mixtures of light elements to obtain a

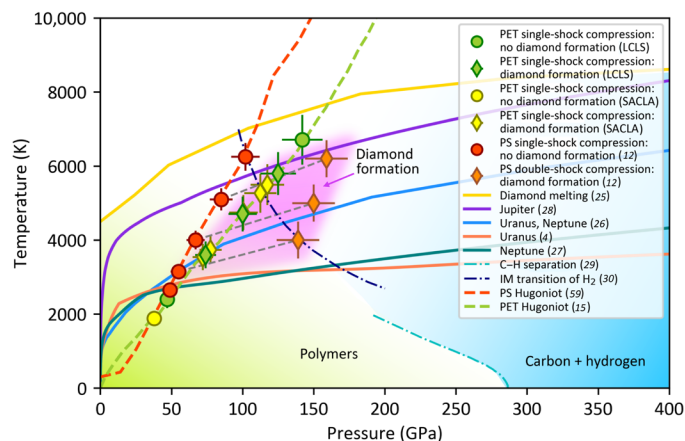


Fig. 4. Phase diagram of mixtures of carbon, hydrogen, and oxygen. The predicted isentropes of Uranus (4, 26), Neptune (26, 27), and Jupiter (28); the diamond melting line (25); the C–H separation line (29); the insulator–metal (IM) transition curve (30); the Hugoniot of PS (59) and PET (15); experimental data of PS in previous works (12, 13); and PET in this work are all presented. The error bars are obtained from the comparison of the XRD measurement with predictions of the scattering intensity from DFT–MD simulations (see Materials and Methods).

most complete picture of the chemical processes in the ice giants. Shock drivers with higher repetition rates will enable studies of many different stoichiometries and better access to kinetics, e.g., via detailed scans of P/T conditions and varying the sample thickness.

Last, the observation of nanodiamonds with tailored sizes in the range of a few nanometers may open the path toward an efficient new source of this material, which exhibits a steadily increasing number of applications in science, medicine, catalysis, and electronics (37). In particular, nanodiamonds of these small sizes with specific color centers may require more effective synthesis methods than currently available to satisfy the needs of applications (38). State-of-the-art high-energy laser systems with hertz repetition rates together with adequate recovery methods (39) may be able to produce large amounts of specifically tailored nanodiamonds from cheap PET. As demonstrated here, this initial material provides access to the diamond formation regime by single-shock compression and therefore does not require sophisticated laser pulse–shaping techniques. Nanodiamonds with specific color centers may be achieved by the corresponding dopant of the initial PET plastics.

MATERIALS AND METHODS

Experimental details

During experiments at LCLS (see similar setup on SACLA in fig. S1 of the Supplementary Materials), a drive laser shock-compressed 100- μm -thick PET foils with a flat top pulse profile, fluences of 15 to 62 J in 8 ns (full width at half maximum), and a spot size of 300 μm in diameter, resulting in intensities between 2.7 and 11 TW/cm^2 . The drive laser creates a rapidly expanding plasma on the front surface of the target, launching a single shock wave into the cold material behind the ablation front. In contrast to the previous experiments on PS (C_8H_8)_n using a double-stage shock (12, 13), a single pulse is sufficient to drive C–H–O samples to similar planetary-relevant states (15). An aluminum coating with a thickness of 1 μm was coated on the sample to prevent low-intensity laser prepulses to preheat the sample, and the reflective metal layer can also be applied to

characterize the shock dynamics with VISAR to constrain pressure and density inside the sample. In front of the aluminum coating was a 9- μm -thick PS ablator.

XRD was performed in an angular range from $2\theta = 22^\circ$ to 72° (corresponding to scattering vector lengths from $q = 1.8$ to 5.6 \AA^{-1}) with ePix detectors (40). For SAXS, a Jungfrau detector (41) located 1165 mm from the target allowed to measure an angular range from $2\theta = 0.24^\circ$ to 1.31° (corresponding to scattering vector lengths from $q = 0.2$ to 1.1 nm^{-1}).

Assuming a stable shock wave transmitting in the sample, the average shock velocity in the compressed sample is given by the transit time via VISAR, as shown in Fig. 1. The pressure and temperature in the sample are then derived from the Hugoniot of PET (15). Those results were cross-checked with the P–T conditions by comparison of the XRD data with calculations from DFT–MD simulations. Both approaches agreed within relative errors of $\pm 10\%$ in temperature and pressure.

SAXS analysis methods

Two SAXS data analysis methods are applied in this work to obtain the size distribution of nanoparticles. The classical SAXS analysis is based on an analytical model. The expected scattering intensity I_{abs} in absolute units can be defined using (21)

$$I_{\text{abs}}(q) = \varphi(1 - \varphi) \cdot (\Delta\rho_{\text{sl}})^2 \cdot V \cdot |F(q)|^2 \cdot S(q) \quad (1)$$

where q is the wave number, φ is the volume fraction of the nanoparticles, $1 - \varphi$ is the volume fraction of the solution, V is the volume of a single nanoparticle, $\Delta\rho_{\text{sl}}$ is the total scattering length density contrast between solids and solutions, and $F(q)$ and $S(q)$ represent the form factor and structure factor, respectively. Considering that the distribution of nanoparticles in the experiments is polydisperse in size and the intensity can be regarded as the average of all size contributions, the form factor $F(q)$ of spherical nanoparticles with a Schulz distribution (23, 24) assuming that the diamonds exist in a uniform liquid background can be expressed as

$$|F(q)|^2 = \frac{\pi^2}{2} \cdot (z + 1)^{-6} \cdot a^{z+7} \cdot G(q) \quad (2)$$

where

$$a = \frac{z+1}{q \cdot R}$$

$$G(q) = a^{-(z+1)} - (4 + a^2)^{-\frac{z+1}{2}} \cdot \cos((z+1) \cdot \arctan(\frac{z}{a})) + (z+1) \cdot (z+2) \cdot (a^{-(z+3)} + (4 + a^2)^{-\frac{z+3}{2}} \cdot \cos((z+3) \cdot \arctan(\frac{z}{a}))) - 2 \cdot (z+1) \cdot (4 + a^2)^{-\frac{z+2}{2}} \cdot \sin((z+2) \cdot \arctan(\frac{z}{a})) \quad (3)$$

Also, $z = 1/p^2 - 1$, $p = \sigma/R$ describes the polydispersity of the nanoparticles. By introducing the repellent potential $U(r)$ of a hard sphere in the Percus–Yevick closure (42–45), the structure factor can be described as

$$S(q) = \frac{1}{1 + 24 \cdot \varphi \cdot \frac{G(2qR)}{2qR}} \quad (4)$$

where

$$a = \frac{(1 + 2\varphi)^2}{(1 - \varphi)^4}$$

$$\beta = -6\varphi \cdot \frac{\left(1 + \frac{\varphi}{2}\right)^2}{(1 - \varphi)^4}$$

$$\gamma = \frac{1}{2}\varphi \cdot \frac{(1 + 2\varphi)^2}{(1 - \varphi)^4}, \quad (5)$$

$$G(A) = \frac{a}{A^2} \cdot (\sin(A) - A \cdot \cos(A)) +$$

$$\frac{\beta}{A^3} \cdot (2A \cdot \sin(A) + (2 - A^2) \cdot \cos(A) - 2) +$$

$$\frac{\gamma}{A^5} \cdot (-A^4 \cdot \cos(A) + 4 \cdot [(3A^2 - 6) \cdot \cos(A) + (A^3 - 6A) \cdot \sin(A) + 6])$$

Therefore, the particle distribution and an associated goodness of fit can be obtained by fitting this analytical model to the experimental data.

In addition, SAXS data can be analyzed using a Monte Carlo technique to fit the experimental data, which is very suitable for complex structures. It is even possible to fit points of an arbitrary radial distribution assuming densely packed spheres with the SAXS analysis program McSAS (46, 47) in the premise of high-quality data with known error and absolute units. It should be considered that each sampling point within the radial distribution function adds another free parameter in the fit, so it is more suitable for data with a wide q range and high dynamic range. Also, this distribution best applies to systems with a single scattering component as in our case (only one type of polydispersed nanoparticles).

DFT-MD simulations

The DFT-MD simulations of diffraction signals in compressed C—H—O samples with various carbon-to-water ratios under different pressure-temperature conditions were compared to experimental XRD data, which can help to predict the demixing of nanodiamonds and residual liquid in the sample. The simulations were performed using the VASP package (48–51), where the Mermin formulation was used to optimize the Helmholtz free energy at a given temperature (52). The electronic density in the simulation box with periodic boundary conditions was represented by a plane wave expansion with a cutoff energy of $E_{\text{cut}} = 1000$ eV. The electron-ion interaction was modeled using the projector augmented wave (PAW) approach, specifically the hard PAW pseudopotentials for hydrogen (H_h, 06Feb2004), carbon (four valence electrons, C_h Feb2004), and oxygen (six valence electrons, O_h Feb2004) as provided with VASP (53, 54). The exchange-correlation functional was taken in generalized gradient approximation in Perdew-Burke-Ernzerhof parametrization (55). The Brillouin zone of the supercell was generally sampled at the Γ point only. The electronic bands were populated using a Fermi distribution at the chosen temperature. The supercell contained atoms of carbon, hydrogen, and oxygen (ratio of C to H₂O was set from 0.31:1 to 2.5:1 where 2.5:1 is the C-to-H₂O ratio of cold PET, and there are always 32 units of H₂O in the supercell), whose movements were calculated using the Hellmann-Feynman forces derived from the electron densities of DFT under the Born-Oppenheimer approximation. The time step was $t = 0.2$ fs, and the DFT-MD run covers a time span of 2 to 4 ps. The ion temperature was controlled by a Nosé-Hoover thermostat (56). The ion structure and therefore

the intensity of the elastic x-ray scattering in this multicomponent system can be obtained from the recorded MD coordinates (57). The expected x-ray scattering intensity I was calculated using

$$I(q) \propto \sum_{ab} \sqrt{x_a x_b} f_a(q) f_b(q) S_{ab}(q) + \sum_a x_a \sum_n (1 - f_{an}(q)^2) \quad (6)$$

where x_a is the atomic fraction of species a (with a being O, C, or H in various C—H—O samples), f_a is the atomic form factor of the whole ion or atom a , and f_{an} is the contribution to f_a caused by the n th electron. S_{ab} denotes the partial structure factors. The first item to the right of proportional sign in Eq. 6 describing the elastic scattering is determined by the Rayleigh weight (54). The second term considers the inelastic scattering as it was treated by Lütgert *et al.* (15).

SUPPLEMENTARY MATERIALS

Supplementary material for this article is available at <https://science.org/doi/10.1126/sciadv.abo0617>

REFERENCES AND NOTES

- L. Zeng, S. B. Jacobsen, D. D. Sasselov, M. I. Petaev, A. Vanderburg, M. Lopez-Morales, J. Perez-Mercader, T. R. Mattsson, G. Li, M. Z. Heising, A. S. Bonomo, M. Damasso, T. A. Berger, H. Cao, A. Levi, R. D. Wordsworth, Growth model interpretation of planet size distribution. *Proc. Natl. Acad. Sci. U.S.A.* **116**, 9723–9728 (2019).
- R. Helled, N. Nettelmann, T. Guillot, Uranus and Neptune: Origin, evolution and internal structure. *Space Sci. Rev.* **216**, 38 (2020).
- R. Chau, S. Hamel, W. J. Nellis, Chemical processes in the deep interior of Uranus. *Nat. Commun.* **2**, 203 (2011).
- M. Bethkenhagen, E. R. Meyer, S. Hamel, N. Nettelmann, M. French, L. Scheibe, C. Ticknor, L. A. Collins, J. D. Kress, J. J. Fortney, R. Redmer, Planetary ices and the linear mixing approximation. *Astrophys. J.* **848**, 67 (2017).
- V. N. Robinson, A. Hermann, Plastic and superionic phases in ammonia–water mixtures at high pressures and temperatures. *J. Phys. Condens. Matter* **32**, 184004 (2020).
- L. R. Benedetti, J. H. Nguyen, W. A. Caldwell, H. Liu, M. Kruger, R. Jeanloz, Dissociation of CH₄ at high pressures and temperatures: Diamond formation in giant planet interiors? *Science* **286**, 100–102 (1999).
- M. Ross, The ice layer in Uranus and Neptune—Diamonds in the sky? *Nature* **292**, 435–436 (1981).
- J. M. McMahon, M. A. Morales, C. Pierleoni, D. M. Ceperley, The properties of hydrogen and helium under extreme conditions. *Rev. Mod. Phys.* **84**, 1607–1653 (2012).
- S. Stanley, J. Bloxham, Numerical dynamo models of Uranus' and Neptune's magnetic fields. *Icarus* **184**, 556–572 (2006).
- R. Redmer, T. R. Mattsson, N. Nettelmann, M. French, The phase diagram of water and the magnetic fields of Uranus and Neptune. *Icarus* **211**, 798–803 (2011).
- K. Soderlund, S. Stanley, The underexplored frontier of ice giant dynamos. *Philos. Trans. R. Soc. A* **378**, 20190479 (2020).
- D. Kraus, J. Vorberger, A. Pak, N. Hartley, L. Fletcher, S. Frydrych, E. Galtier, E. Gamboa, D. Gericke, S. H. Glenzer, E. Granados, M. J. MacDonald, A. J. M. Kinnon, E. E. M. McBride, I. Nam, P. Neumayer, M. Roth, A. M. Saunders, A. K. Schuster, P. Sun, T. van Driel, T. Döppner, R. W. Falcone, Formation of diamonds in laser-compressed hydrocarbons at planetary interior conditions. *Nat. Astron.* **1**, 606–611 (2017).
- D. Kraus, N. Hartley, S. Frydrych, A. Schuster, K. Rohatsch, M. Rödel, T. Cowan, S. Brown, E. Cunningham, T. Van Driel, L. B. Fletcher, E. Galtier, E. J. Gamboa, A. L. Garcia, D. O. Gericke, E. Granados, P. A. Heimann, H. J. Lee, M. J. MacDonald, A. J. MacKinnon, E. E. McBride, I. Nam, P. Neumayer, A. Pak, A. Pelka, I. Prencipe, A. Ravasio, R. Redmer, A. M. Saunders, M. Schölmerich, M. Schörner, P. Sun, S. J. Turner, A. Zettl, R. W. Falcone, S. H. Glenzer, T. Döppner, J. Vorberger, High-pressure chemistry of hydrocarbons relevant to planetary interiors and inertial confinement fusion. *Phys. Plasmas* **25**, 056313 (2018).
- A. K. Schuster, N. Hartley, J. Vorberger, T. Döppner, T. Van Driel, R. Falcone, L. Fletcher, S. Frydrych, E. Galtier, E. Gamboa, D. O. Gericke, A. Schuster, A. Benuzzi-Mounaix, A. J. MacKinnon, E. E. McBride, I. Nam, P. Neumayer, A. Pak, I. Prencipe, K. Voigt, A. M. Saunders, P. Sun, D. Kraus, Measurement of diamond nucleation rates from hydrocarbons at conditions comparable to the interiors of icy giant planets. *Phys. Rev. B* **101**, 054301 (2020).
- J. Lütgert, J. Vorberger, N. Hartley, K. Voigt, M. Rödel, A. Schuster, A. Benuzzi-Mounaix, S. Brown, T. Cowan, E. Cunningham, T. Döppner, R. W. Falcone, L. B. Fletcher, E. Galtier, S. H. Glenzer, A. L. Garcia, D. O. Gericke, P. A. Heimann, H. J. Lee, E. E. McBride, A. Pelka, I. Prencipe, A. M. Saunders, M. Schölmerich, M. Schörner, P. Sun, T. Vinci, A. Ravasio, D. Kraus, Measuring the structure and equation of state of polyethylene terephthalate at megabar pressures. *Sci. Rep.* **11**, 12883 (2021).

16. O. Glatter, O. Kratky, H. Kratky, *Small Angle X-ray Scattering* (Academic Press, 1982).
17. B. Nagler, B. Arnold, G. Bouchard, R. F. Boyce, R. M. Boyce, A. Callen, M. Campell, R. Curiel, E. Galtier, J. Garofoli, E. Granados, J. Hastings, G. Hays, P. Heimann, R. W. Lee, D. Milathianaki, L. Plummer, A. Schropp, A. Wallace, M. Welch, W. White, Z. Xing, J. Yin, J. Young, U. Zastrau, H. J. Lee, The matter in extreme conditions instrument at the Linac coherent light source. *J. Synchrotron Radiat.* **22**, 520–525 (2015).
18. S. H. Glenzer, L. Fletcher, E. Galtier, B. Nagler, R. Alonso-Mori, B. Barbrel, S. Brown, D. Chapman, Z. Chen, C. Curry, F. Fiuzza, E. Gamboa, K. Gauthier, D. O. Gericke, A. Gleason, S. Goede, E. Granados, P. Heimann, J. Kim, D. Kraus, M. J. MacDonald, A. J. Mackinnon, R. Mishra, A. Rivasio, C. Roedel, P. Sperling, W. Schumaker, Y. Y. Tsui, J. Vorberger, U. Zastrau, A. Fry, W. E. White, J. B. Hasting, H. J. Lee, Matter under extreme conditions experiments at the Linac Coherent Light Source. *J. Phys. B* **49**, 092001 (2016).
19. M. Yabashi, H. Tanaka, T. Ishikawa, Overview of the SACL facility. *J. Synchrotron Radiat.* **22**, 477–484 (2015).
20. Y. Inubushi, T. Yabuuchi, T. Togashi, K. Sueda, K. Miyanishi, Y. Tange, N. Ozaki, T. Matsuo, R. Kodama, T. Osaka, S. Matsuyama, K. Yamauchi, H. Yumoto, T. Koyama, H. Ohashi, K. Tono, M. Yabashi, Development of an experimental platform for combinative use of an XFEL and a high-power nanosecond laser. *Appl. Sci.* **10**, 2224 (2020).
21. A. Guinier, G. Fournet, K. L. Yudowitch, *Small-Angle Scattering of X-Rays* (John Wiley & Sons, 1955).
22. A. Monshi, M. R. Foroughi, M. R. Monshi, Modified Scherrer equation to estimate more accurately nano-crystallite size using XRD. *World J. Nano. Sci. Eng.* **02**, 154–160 (2012).
23. M. Kotlarchyk, S. H. Chen, Analysis of small angle neutron scattering spectra from polydisperse interacting colloids. *J. Chem. Phys.* **79**, 2461–2469 (1983).
24. J. Als-Nielsen, D. Mcmorrow, *Elements of Modern X-ray Physics* (John Wiley & Sons, 2011).
25. X. Wang, S. Scandolo, R. Car, Carbon phase diagram from ab initio molecular dynamics. *Phys. Rev. Lett.* **95**, 185701 (2005).
26. T. Guillot, D. Gautier, Giant planets. *Treatise Geophys.* **10**, 439–464 (2007).
27. L. Scheibe, N. Nettelmann, R. Redmer, Thermal evolution of Uranus and Neptune—I. Adiabatic models. *Astron. Astrophys.* **632**, A70 (2019).
28. N. Nettelmann, N. Movshovitz, D. Ni, J. Fortney, E. Galanti, Y. Kaspi, R. Helled, C. Mankovich, S. Bolton, Theory of Figures to the 7th order and the interiors of Jupiter and Saturn. arXiv:2110.15452 (2021).
29. G. Gao, A. R. Oganov, Y. Ma, H. Wang, P. Li, Y. Li, T. litaka, G. Zou, Dissociation of methane under high pressure. *J. Chem. Phys.* **133**, 144508 (2010).
30. R. S. McWilliams, D. A. Dalton, M. F. Mahmood, A. F. Goncharov, Optical properties of fluid hydrogen at the transition to a conducting state. *Phys. Rev. Lett.* **116**, 255501 (2016).
31. S. T. Weir, A. C. Mitchell, W. J. Nellis, Metallization of fluid molecular hydrogen at 140 GPa (1.4 Mbar). *Phys. Rev. Lett.* **76**, 1860 (1996).
32. M. Eremets, I. Troyan, Conductive dense hydrogen. *Nat. Mater.* **10**, 927–931 (2011).
33. P. M. Celliers, M. Millot, S. Brygoo, R. S. McWilliams, D. E. Fratanduono, J. R. Rygg, A. F. Goncharov, P. Loubeyre, J. H. Eggert, J. L. Peterson, N. B. Meezan, S. L. Pape, G. W. Collins, R. Jeanloz, R. J. Hemley, Insulator-metal transition in dense fluid deuterium. *Science* **361**, 677–682 (2018).
34. M. Knudson, M. Desjarlais, A. Becker, R. Lemke, K. Cochran, M. Savage, D. Bliss, T. Mattsson, R. Redmer, Direct observation of an abrupt insulator-to-metal transition in dense liquid deuterium. *Science* **348**, 1455–1460 (2015).
35. V. E. Fortov, R. I. Ilkaev, V. A. Arinin, V. V. Burtzev, V. A. Golubev, I. L. Iosilevskiy, V. V. Khrustalev, A. L. Mikhailov, M. A. Mochalov, V. Y. Ternovoi, M. V. Zhernokletov, Phase transition in a strongly nonideal deuterium plasma generated by quasi-isentropic compression at megabar pressures. *Phys. Rev. Lett.* **99**, 185001 (2007).
36. M. Millot, F. Coppari, J. R. Rygg, A. C. Barrios, S. Hamel, D. C. Swift, J. H. Eggert, Nanosecond x-ray diffraction of shock-compressed superionic water ice. *Nature* **569**, 251–255 (2019).
37. V. N. Mochalin, O. Shenderova, D. Ho, Y. Gogotsi, The properties and applications of nanodiamonds. *Nat. Nanotechnol.* **7**, 11–23 (2012).
38. J.-C. Arnault, *Nanodiamonds* (Elsevier, 2017).
39. M. G. Gorman, D. McGonigle, S. J. Tracy, S. M. Clarke, C. A. Bolme, A. E. Gleason, S. J. Ali, S. Hok, C. W. Greeff, P. G. Heighway, K. Hulpach, B. Glam, E. Galtier, H. J. Lee, J. S. Wark, J. H. Eggert, J. K. Wicks, R. F. Smith, Recovery of a high-pressure phase formed under laser-driven compression. *Phys. Rev. B* **102**, 024101 (2020).
40. G. Blaj, A. Dragone, C. Kenney, F. Abu-Nimeh, P. Caragiulo, D. Doering, M. Kwiatkowski, B. Markovic, J. Pines, M. Weaver, S. Boutet, G. Carini, C.-E. Chang, P. Hart, J. Hasi, M. Hayes, R. Herbst, J. Koglin, K. Nakahara, J. Segal, G. Haller, Performance of ePix10K, a high dynamic range, gain auto-ranging pixel detector for FELs. *AIP Conf. Proc.* **2054**, 060662 (2019).
41. A. Mozzanica, M. Andrä, R. Barten, A. Bergamaschi, S. Chirioti, M. Brückner, R. Dinapoli, E. Fröjd, D. Greiffenberg, F. Leonarski, C. Lopez-Cuenca, D. Mezza, S. Redford, C. Ruder, B. Schmitt, X. Shi, D. Thattil, G. Tinti, S. Vetter, J. Zhang, The JUNGFRUA detector for applications at synchrotron light sources and XFELs. *Synchrotron Radiat. News* **31**, 16–20 (2018).
42. M. Wertheim, Exact solution of the Percus-Yevick integral equation for hard spheres. *Phys. Rev. Lett.* **10**, 321–323 (1963).
43. J. K. Percus, G. J. Yevick, Analysis of classical statistical mechanics by means of collective coordinates. *Phys. Rev.* **110**, 1–13 (1958).
44. D. J. Kinning, E. L. Thomas, Hard-sphere interactions between spherical domains in diblock copolymers. *Macromolecules* **17**, 1712–1718 (1984).
45. J. S. Pedersen, Determination of size distribution from small-angle scattering data for systems with effective hard-sphere interactions. *J. Appl. Cryst.* **27**, 595–608 (1994).
46. B. R. Pauw, J. S. Pedersen, S. Tardif, M. Takata, B. B. Iversen, Improvements and considerations for size distribution retrieval from small-angle scattering data by Monte Carlo methods. *J. Appl. Cryst.* **46**, 365–371 (2013).
47. I. Breßler, B. R. Pauw, A. F. Thünemann, McSAS: Software for the retrieval of model parameter distributions from scattering patterns. *J. Appl. Cryst.* **48**, 962–969 (2015).
48. G. Kresse, J. Hafner, Ab initio molecular dynamics for liquid metals. *Phys. Rev. B* **47**, 558–561 (1993).
49. G. Kresse, J. Hafner, Ab initio molecular-dynamics simulation of the liquid-metal–amorphous-semiconductor transition in germanium. *Phys. Rev. B* **49**, 14251–14269 (1994).
50. G. Kresse, J. Furthmüller, Efficiency of ab-initio total energy calculations for metals and semiconductors using a plane-wave basis set. *Comput. Mater. Sci.* **6**, 15–50 (1996).
51. G. Kresse, J. Furthmüller, Efficient iterative schemes for ab initio total-energy calculations using a plane-wave basis set. *Phys. Rev. B* **54**, 11169–11186 (1996).
52. N. D. Mermin, Thermal properties of the inhomogeneous electron gas. *Phys. Rev.* **137**, A1441–A1443 (1965).
53. P. E. Blöchl, Projector augmented-wave method. *Phys. Rev. B* **50**, 17953–17979 (1994).
54. G. Kresse, D. Joubert, From ultrasoft pseudopotentials to the projector augmented-wave method. *Phys. Rev. B* **59**, 1758–1775 (1999).
55. J. P. Perdew, K. Burke, M. Ernzerhof, Generalized gradient approximation made simple. *Phys. Rev. Lett.* **77**, 3865–3868 (1996).
56. N. Shuichi, Constant temperature molecular dynamics methods. *Prog. Theoret. Phys. Suppl.* **103**, 1–46 (1991).
57. K. Wünsch, J. Vorberger, G. Gregori, D. O. Gericke, X-ray scattering as a probe for warm dense mixtures and high-pressure miscibility. *Europhys. Lett.* **94**, 25001 (2011).
58. M. Rödel, “Coherent x-ray diffraction of laser-driven matter,” thesis, Technische Universität Dresden (2022).
59. M. A. Barrios, D. G. Hicks, T. R. Boehly, D. E. Fratanduono, J. H. Eggert, P. M. Celliers, G. W. Collins, D. D. Meyerhofer, High-precision measurements of the equation of state of hydrocarbons at 1–10 Mbar using laser-driven shock waves. *Phys. Plasmas* **17**, 082702 (2010).

Acknowledgments

Funding: Use of the Linac Coherent Light Source (LCLS), SLAC National Accelerator Laboratory, is supported by the U.S. Department of Energy, Office of Science, Office of Basic Energy Sciences under contract no. DE-AC02-76SF00515. The MEC instrument is supported by the U.S. Department of Energy, Office of Science, Office of Fusion Energy Sciences under contract no. SF00515. The XFEL experiments on SACL were performed using BL3 at the EHS with the approvals of the Japan Synchrotron Radiation Research Institute (JASRI) (proposal no. 2019A8070) and the Institute of Laser Engineering, Osaka University. This work was supported by the Helmholtz Association under VH-NG-1141 and ERC-RA-0041. Z.H. acknowledges the financial support from the China Scholarship Council. SLAC HED acknowledges the U.S. Department of Energy, Office of Science, Office of Fusion Energy Sciences grant no. FWP 100182, and N.J.H. and E.E.M. were supported by the Panofsky Fellowship awarded to E.E.M. A.E.G. and S.P. also acknowledge support from 2019 DOE FES ECA. G.D.G. acknowledges support from the DOE NNSA SSGF program under DE-NA0003960. M.B. was supported by the European Horizon 2020 programme within the Marie Skłodowska-Curie actions (xICE grant no. 894725). M.F. and R.R. acknowledge support by the Deutsche Forschungsgemeinschaft (DFG) within the FOR 2440. **Author contributions:** Project planning and experimental design: D.Kr., A.R., E.E.M., A.E.G., H.J.L., E.G., B.N., N.J.H., R.R., M.B., M.F., J.V., M.R., N.O., N.K., K.K., and S.H.G. Carrying out experiments: J.L., M.G.S., O.S.H., A.K.S., K.V., E.E.M., B.N., H.J.L., N.J.H., A.E.G., S.P., E.G., D.Kh., A.D., B.O.-O., G.D.G., C.S., M.R., D.C., T.Y., K.M., N.O., N.K., K.K., K.S., J.-A.H., Y.I., T.T., M.Y., A.R., and D.Kr. Data analysis and discussions: Z.H., D.Kr., A.R., M.R., J.L., M.G.S., L.M.V.Z., B.H., D.R., O.S.H., A.K.S., K.V., D.C., C.Q., M.B., M.F., A.B., R.R., T.E.C., T.V., E.E.M., N.J.H., and J.-A.H. DFT calculations: J.V. Writing—original draft: Z.H. and D.Kr. Writing—review and editing: Z.H., D.Kr., M.R., J.L., J.V., M.G.S., N.J.H., O.S.H., B.H., A.B., M.F., G.D.G., A.K.S., M.B., S.P., and R.R. **Competing interests:** The authors declare that they have no competing interests. **Data and materials availability:** All data needed to evaluate the conclusions in the paper are present in the paper and/or the Supplementary Materials and at <https://doi.org/10.14278/rodare.1696>.

Submitted 27 January 2022

Accepted 18 July 2022

Published 2 September 2022

10.1126/sciadv.abo0617

Diamond formation kinetics in shock-compressed C#H#O samples recorded by small-angle x-ray scattering and x-ray diffraction

Zhiyu He, Melanie Rdel, Julian Ltgert, Armin Bergermann, Mandy Bethkenhagen, Deniza Chekrygina, Thomas E. Cowan, Adrien Descamps, Martin French, Eric Galtier, Arianna E. Gleason, Griffin D. Glenn, Siegfried H. Glenzer, Yuichi Inubushi, Nicholas J. Hartley, Jean-Alexis Hernandez, Benjamin Heuser, Oliver S. Humphries, Nobuki Kamimura, Kento Katagiri, Dimitri Khaghani, Hae Ja Lee, Emma E. McBride, Kohei Miyanishi, Bob Nagler, Benjamin Ofori-Okai, Norimasa Ozaki, Silvia Pandolfi, Chongbing Qu, Divyanshu Ranjan, Ronald Redmer, Christopher Schoenwaelder, Anja K. Schuster, Michael G. Stevenson, Keiichi Sueda, Tadashi Togashi, Tommaso Vinci, Katja Voigt, Jan Vorberger, Makina Yabashi, Toshinori Yabuuchi, Lisa M. V. Zinta, Alessandra Ravasio, and Dominik Kraus

Sci. Adv., **8** (35), eabo0617.
DOI: 10.1126/sciadv.abo0617

View the article online

<https://www.science.org/doi/10.1126/sciadv.abo0617>

Permissions

<https://www.science.org/help/reprints-and-permissions>

Use of this article is subject to the [Terms of service](#)

Science Advances (ISSN) is published by the American Association for the Advancement of Science. 1200 New York Avenue NW, Washington, DC 20005. The title *Science Advances* is a registered trademark of AAAS.

Copyright © 2022 The Authors, some rights reserved; exclusive licensee American Association for the Advancement of Science. No claim to original U.S. Government Works. Distributed under a Creative Commons Attribution License 4.0 (CC BY).